

SURE: Safe Uncertainty-Aware Robot-Environment Interaction using Trajectory Optimization

Zhuocheng Zhang*, Haizhou Zhao*†, Xudong Sun*, Aaron M. Johnson*‡, Majid Khadiv*

*Technical University of Munich (TUM), Germany. †New York University (NYU), USA.

‡Carnegie Mellon University (CMU), USA.

Abstract—Robotic tasks involving contact interactions pose significant challenges for trajectory optimization due to discontinuous dynamics. Conventional formulations typically assume deterministic contact events, which limit robustness and adaptability in real-world settings. In this work, we propose SURE, a robust trajectory optimization framework that explicitly accounts for contact timing uncertainty. By allowing multiple trajectories to branch from possible pre-impact states and later rejoin a shared trajectory, SURE achieves both robustness and computational efficiency within a unified optimization framework. We evaluate SURE on two representative tasks with unknown impact times. In a cart–pole balancing task involving uncertain wall location, SURE achieves an average improvement of 21.6% in success rate when branch switching is enabled during control. In an egg-catching experiment using a robotic manipulator, SURE improves the success rate by 40%. These results demonstrate that SURE substantially enhances robustness compared to conventional nominal formulations. A supplementary video demonstrating the results is available [here](#).

I. INTRODUCTION

Locomotion and manipulation tasks inherently involve intermittent contact with the environment. These changing contact conditions are particularly challenging because they introduce discrete switches in the system dynamics, resulting in a hybrid dynamical system [18]. When trajectory optimization is applied to such hybrid systems, the resulting formulation typically takes the form of a mathematical program with complementarity constraints (MPCC) [30, 28, 20, 3] or a mixed-integer optimization problem [8, 1, 33, 29, 7].

Most recent trajectory optimization approaches for contact-rich problems adopt hierarchical formulations [37], in which contact planning and whole-body motion generation are treated separately. These methods typically assume deterministic contact timings [14, 9]. In practice, however, such assumptions are overly restrictive: environmental perception is inherently uncertain, and both modeling errors and end-effector tracking inaccuracies during contact establishment can cause discrepancies between planned and actual contact times. To mitigate these effects, existing frameworks often rely on the inherent robustness of model predictive control (MPC) through frequent replanning [32, 25, 26, 38]. Nevertheless, contact switches introduce very fast dynamics that cannot be captured by the re-planning frequency of the MPC controllers, underscoring the need for a more systematic framework that explicitly addresses contact-timing uncertainty.

The primary contribution of this work is the development of a robust trajectory optimization framework, termed SURE, for

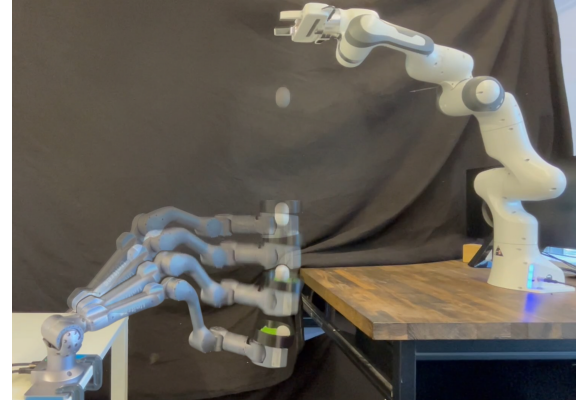


Fig. 1. Illustration of the egg-catching task. The Unitree Z1 robot arm attempts to catch a falling egg while minimizing impact. The egg serves both as the test object and as a passive sensor for detecting contact forces. In this task, timing deviations on the order of milliseconds can significantly affect performance, highlighting the importance of robustness to contact-timing uncertainties.

hybrid systems with uncertain contact timing. The framework introduces a branching phase, in which nodes can branch and subsequently rejoin a common final trajectory, thereby achieving both robustness and computational efficiency. Using two case studies, we demonstrate the improved robustness of the proposed approach compared to nominal trajectory optimization and analyze different implementations.

The remainder of this paper is organized as follows. Section II reviews related work. Section III introduces the nominal trajectory optimization formulation. Section IV presents the proposed robust trajectory optimization approach. Section V-A applies the proposed method to a cart–pole system with wall impacts to evaluate and compare its performance. Section V-B applies the proposed method to a ball-catching robot, demonstrating a more complex system and its translation to real-world hardware experiments. Section VI concludes the paper and discusses potential directions for future work.

II. RELATED WORK

Robust and stochastic optimal control methods have been extensively explored for contact-rich robotic systems [12, 16, 13, 31, 10, 24]. For example, [10] models contact parameters as random variables and minimizes the expected residual of complementarity constraints, yielding trajectories that are more resilient to variations in terrain and friction. [16] introduces a risk-sensitive controller that adapts end-effector impedance in response to disturbances, thereby mitigating un-

certain impact effects. Although these methods offer valuable theoretical insights and enhanced safety, they take into account the contact timing uncertainties only in the feedback control design. In particular, with delayed contact events (e.g., late foot touchdown), controller performance remains limited without adapting the desired trajectory. [36] handles timing uncertainty by constraining predicted post-impact states, while [34] resorts to a reference-spreading mechanism. However, such an instantaneous controller without a prediction horizon may result in myopic decisions. [40, 41] leverage the saltation matrix [21], which provides a closed-form representation of how discrete hybrid events influence trajectory stability, to explicitly shape hybrid transitions and mitigate contact uncertainty. However, this is a local linearization and does not consider what control should be applied in the event of a contact timing mismatch. A similar limitation applies to [19], where actions were planned to reduce changes in uncertainty between time steps. [15] accounts for contact uncertainty by jointly optimizing trajectories over multiple ground-height disturbances, enforcing shared control inputs to achieve robustness without online replanning. More recently, [39] introduces a robust trajectory optimization formulation to handle contact-timing uncertainty; however, this method does not capture long-term optimality or dependencies on post-impact events.

In the realm of reinforcement learning, several studies have explored uncertainty-aware control strategies. [4] proposes a variable-gain PD control approach within an RL framework, improving robustness under variations in the contact event. [23, 5] further enhance policy robustness by injecting noise during training to emulate parameter and environmental uncertainties. However, RL-based methods generally lack mechanisms to enforce hard constraints on internal variables such as impact forces, raising potential safety concerns. Despite these limitations, principles from RL can still inform and inspire the design of more robust optimization-based control frameworks.

III. NOMINAL TRAJECTORY OPTIMIZATION

In this section, we present the formulation of the nominal trajectory optimization using multiple shooting [27], which assumes that contact occurs at a deterministic time. The trajectory starts from the initial state \mathbf{x}_0 , under control \mathbf{u} , and is discretized into N shooting nodes, Fig. 2a. We assume that the contact occurs at the node indexed by c . The trajectory optimization problem can then be formulated as follows:

$$\begin{aligned} \min_{\mathbf{x}, \mathbf{u}, \Delta t} \quad & \sum_{i=0}^{N-1} L_i(\mathbf{x}_i, \mathbf{u}_i, \Delta t_i) + L_N(\mathbf{x}_N) & (1a) \\ \text{s.t.} \quad & \forall i \in [0, N] : \quad \mathbf{w}_i(\mathbf{x}_i, \mathbf{u}_i) = 0, & (1b) \\ & \mathbf{h}_i(\mathbf{x}_i, \mathbf{u}_i) \leq 0, & (1c) \\ & \forall i \notin \{c, N\} : \quad \mathbf{f}_i(\mathbf{x}_i, \mathbf{u}_i, \mathbf{x}_{i+1}, \Delta t_i) = 0, & (1d) \\ & g(\mathbf{x}_i) > 0, & (1e) \\ & i = c : \quad \mathbf{x}_{i+1} = R(\mathbf{x}_i), & (1f) \\ & g(\mathbf{x}_i) = 0, & (1g) \\ & \Delta t \in [\Delta t_{\min}, \Delta t_{\max}]. & (1h) \end{aligned}$$

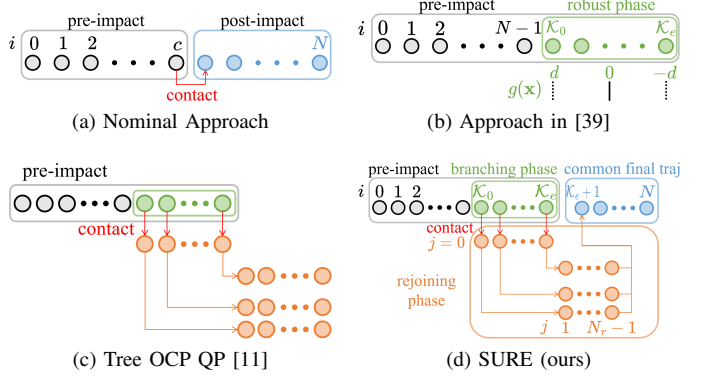


Fig. 2. (a) The nominal trajectory optimization problem. The contact occurs at the node indexed by c , separating the pre- and post-impact phases. (b) The method in [39], where the contact may occur at any node within the robust phase. (c) The Tree OCP QP [11], which is a brute-force formulation that requires an extremely large number of nodes, leading to high computational cost. (d) SURE trajectory optimization problem. The gray nodes represent the pre-contact trajectory, the green nodes correspond to the branching phase (serving the same role as the robust phase in (b)), and the blue nodes denote the common final trajectory. Together, they form the common trajectory. The orange nodes represent the branch trajectories, each diverging from a branching node and rejoining the common final trajectory, composing the rejoining phase.

Here, Δt_i denotes the time interval between nodes, varying within the bounds specified in (1h); L_N is the terminal cost; L_i is the running cost; \mathbf{w} and \mathbf{h} represent the state-input equality and inequality constraints, respectively; \mathbf{f} specifies the discrete dynamics; g is the guard function, whose value determines the triggering condition of the contact event (contact occurs at $g = 0$, while $g > 0$ holds at all other times); and R is the impact or reset function.

IV. SURE TRAJECTORY OPTIMIZATION

The formulation in (1) assumes a deterministic contact event. However, this assumption is often unrealistic due to modeling mismatches or perception errors. In such cases, the trajectory obtained from (1) cannot accommodate the timing uncertainty: if the contact occurs earlier or later than expected, it may cause a large impact or even lead to instability.

A. Motivation

To account for contact uncertainty, [39] proposed a robust method to address this issue. However, unlike the nominal formulation, it cannot generate a trajectory that explicitly reaches the terminal state (Fig. 2b). Instead, the trajectory terminates at the latest possible contact time, and the subsequent motion depends on how the system replans. Intuitively, this method ensures that the post-contact condition is not overly unfavorable, but it does not provide a concrete plan for reaching the terminal state.

Another approach would be to compute all possible trajectories branching from each possible contact nodes to the terminal states (Fig. 2c), as described by the Tree Optimal Control Problem (OCP) Quadratic Programming (QP) formulation in [11]. However, this brute-force approach drastically

increases the computational complexity of the trajectory optimization problem, making it impractical for systems with a large number of decision variables.

In light of this, our objective is to develop a robust trajectory optimization framework that accounts for uncertainty while avoiding excessive computational complexity.

B. SURE Formulation

Similar to the robust phase in [39], we construct a branching phase \mathcal{K} , which includes all the possible pre-impact nodes. To address the drawback of [39], we force these branches to eventually rejoin a common final trajectory. From each node in the branching phase, we generate a rejoining phase trajectory, each of which ends at the start of this common final trajectory, as shown in Fig. 2d. For trajectories with multiple contact transitions, this process is repeated for each.

In this way, uncertainty is explicitly accounted for, while avoiding the need to plan separate trajectories from each post-impact state to the terminal state. Instead, all branches rejoin a common state, from which they evolve jointly toward the terminal state. This strategy trades a degree of optimality for substantially improved computational efficiency, as it greatly reduces the number of decision variables.

The SURE trajectory optimization problem under uncertain contact timing is formulated as follows:

$$\min_{\mathbf{x}, \mathbf{u}, \Delta t, d} \sum_{i=0}^{N-1} L_i(\mathbf{x}_i, \mathbf{u}_i, \Delta t_i) + \sum_{i \in \mathcal{K}} \sum_{j=0}^{N_r} L_{i,j}(\mathbf{x}_{i,j}, \mathbf{u}_{i,j}, \Delta t_{i,j}) + L_N(\mathbf{x}_N) \quad (2a)$$

$$\text{s.t. } \forall i \in [0, N] : \mathbf{w}_i(\mathbf{x}_i, \mathbf{u}_i) = 0, \quad (2b)$$

$$\mathbf{h}_i(\mathbf{x}_i, \mathbf{u}_i) \leq 0, \quad (2c)$$

$$\forall i \notin \{\mathcal{K}_e, N\} : \mathbf{f}_i(\mathbf{x}_i, \mathbf{u}_i, \mathbf{x}_{i+1}, \Delta t_i) = 0, \quad (2d)$$

$$\forall i \in \mathcal{K} : \mathbf{x}_{i,0} = R(\mathbf{x}_i), \quad (2e)$$

$$\mathbf{x}_{i,N_r} = \mathbf{x}_{\mathcal{K}_e+1}, \quad (2f)$$

$$\forall j \in [0, N_r - 1] : \quad (2g)$$

$$\mathbf{f}_{i,j}(\mathbf{x}_{i,j}, \mathbf{u}_{i,j}, \mathbf{x}_{i,j+1}, \Delta t_{i,j}) = 0, \quad (2g)$$

$$\mathbf{w}_{i,j}(\mathbf{x}_{i,j}, \mathbf{u}_{i,j}) = 0, \quad (2h)$$

$$\mathbf{h}_{i,j}(\mathbf{x}_{i,j}, \mathbf{u}_{i,j}) \leq 0, \quad (2i)$$

$$i = \mathcal{K}_0 : \quad g(\mathbf{x}_i) = d, \quad (2j)$$

$$i = \mathcal{K}_e : \quad g(\mathbf{x}_i) = -d, \quad (2k)$$

$$\forall i < \mathcal{K}_0 : \quad g(\mathbf{x}_i) > d, \quad (2l)$$

$$d \in [d_{\min}, d_{\max}], \quad (2m)$$

$$\Delta t \in [\Delta t_{\min}, \Delta t_{\max}]. \quad (2n)$$

All nodes can be classified into two categories: (1) nodes on the common trajectory (with a single subscript index, e.g., \mathbf{x}_i) and (2) nodes in the rejoining phase (with two subscript indices, e.g., $\mathbf{x}_{i,j}$).
On the common trajectory, \mathcal{K}_0 and \mathcal{K}_e denote the indices of the first and last nodes in the branching phase, respectively.

The variable d denotes half the width of the uncertainty range. At $i = \mathcal{K}_0$, the earliest possible contact, we require $g(\mathbf{x}_i) = d$, (2j), while at $i = \mathcal{K}_e$, the latest possible contact, we require

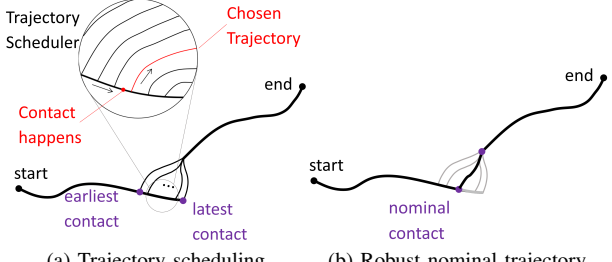


Fig. 3. Illustrations of (a) trajectory scheduling, and (b) the robust nominal trajectory. Trajectory scheduling utilizes all optimized trajectories obtained from the robust approach, whereas the robust nominal trajectory corresponds to the middle branch selected from these solutions.

$g(\mathbf{x}_i) = -d$, (2k). Each node in the branching phase represents a pre-contact state, and we apply a state transition to compute the corresponding post-impact state which is then the initial state on the corresponding branch, (2e).

In the rejoining phase, each branch contains $N_r + 1$ nodes, indexed by $j = 0, 1, \dots, N_r$. Node $\mathbf{x}_{i,j}$ denotes the j -th node on the branch originating from node $i \in \mathcal{K}$. The contact-related cost and constraints are incorporated into $L_{i,j}$ as well as (2h) and (2i). At $j = N_r$, the branch node rejoins the common final trajectory at the node with index $i = \mathcal{K}_e + 1$, (2f).

In practice, the half-width of the uncertainty range, d , can be set as a fixed but tunable parameter, or d can also be treated as a decision variable and incorporated into the cost function. In that case, the solver aims to identify the largest possible uncertainty region over which the system remains robust.

Another parameter that influences robustness is the number of branches, $|\mathcal{K}|$. On the one hand, for the sake of computational efficiency, it is desirable to keep the number of decision variables as small as possible. On the other hand, increasing the number of branches generally improves the robustness of the resulting trajectory. Therefore, a proper trade-off must be found.

C. Application of Solution Trajectories for Control

By solving the trajectory optimization problem in (2), we obtain a family of trajectories corresponding to different possible contact timings. During control, these trajectories can be used as references to guide the system's motion. Depending on whether a sensor is available to detect the contact, there are two ways to exploit these trajectories.

1) *Trajectory Scheduling*: When a sensor is available to detect contact, the reference trajectory can be switched according to the detected contact time, a strategy referred to as *trajectory scheduling* (Fig. 3a). Initially, the system follows the common pre-impact trajectory. Once it enters the branching phase, if contact does not occur, the system continues along the common trajectory. When contact does occur, the scheduler selects the nearest subsequent trajectory as the new reference and guides the system to the terminal state.

2) *Robust Nominal Trajectory*: If no sensor is available for contact detection, having multiple trajectories is still beneficial. By introducing additional decision variables and constraints,

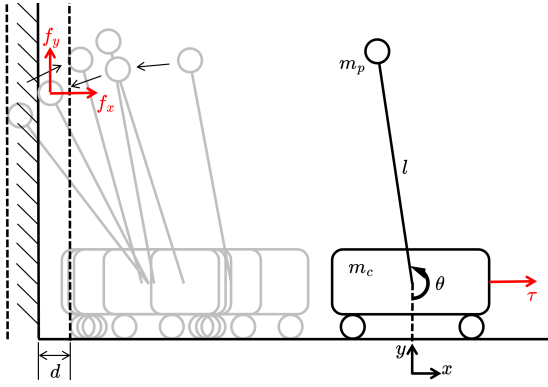


Fig. 4. Illustration of the cart-pole system with wall contact. The cart-pole starts from an initially disturbed state and, due to limited control input, moves toward the wall to induce an impact that reverses the pole's velocity. After the impact, the system seeks to regain balance and return to the desired position. The wall position is uncertain within a range of $\pm d$.

the desired trajectory before the contact event can also be reshaped to reduce the worst-case impact within the uncertainty region. As a result, selecting a branch among these trajectories is expected to yield improved worst-case performance than the nominal trajectory, even though performance in some specific cases may degrade. It is reasonable to choose the middle branch, as it is located at almost equal distance to the extremes of the uncertainty set and thus represents the most representative trajectory. This trajectory branches from index $i = \lceil (\mathcal{K}_0 + \mathcal{K}_e)/2 \rceil$ and is referred to as the *robust nominal trajectory* (Fig. 3b).

V. CASE STUDIES

In this section, we present two case studies to evaluate the trajectories generated by SURE and compare them with those obtained using the nominal formulation. All trajectory optimization problems are formulated and solved using the CasADi framework [2] through its Opti stack interface. The resulting nonlinear programming (NLP) problems are solved using IPOPT [35].

A. Case Study I: Cart-Pole System with Wall

In this case study, a cart-pole system utilizes contact with a wall to stabilize itself under disturbances, while the wall position remains uncertain, as shown in Fig. 4. The dynamics of the system are governed by the following equation:

$$\underbrace{\begin{bmatrix} m_c + m_p & m_p l \cos \theta \\ m_p l \cos \theta & m_p l^2 \end{bmatrix}}_{M(\mathbf{q})} \ddot{\mathbf{q}} + \underbrace{m_p l \sin \theta \begin{bmatrix} -\dot{\theta}^2 \\ g \end{bmatrix}}_{H(\mathbf{q}, \dot{\mathbf{q}})} = \begin{bmatrix} 1 \\ 0 \end{bmatrix} \tau + \underbrace{\begin{bmatrix} 1 & 0 \\ l \cos \theta & l \sin \theta \end{bmatrix}}_{J_c^\top} \mathbf{F} \quad (3)$$

where $\mathbf{q} = [x, \theta]^\top$ denotes the generalized coordinates of the system, with x representing the cart position and θ the pole angle. $m_c = 0.3$ kg and $m_p = 1.0$ kg are the masses of the cart and the pole, respectively, while $l = 0.4$ m is the pole length,

with its mass concentrated at the tip. The input to the system is the external force τ acting on the cart. The term $M(\mathbf{q})$ denotes the mass matrix, and $H(\mathbf{q}, \dot{\mathbf{q}})$ contains the Coriolis, centrifugal, and gravitational terms. The contact Jacobian of the pole tip is denoted by $J_c \in \mathbb{R}^{2 \times 2}$, and the wall reaction force is represented by $\mathbf{F} = [f_x, f_y]^\top \in \mathbb{R}^2$.

For the impact model, the wall is assumed to have a friction coefficient $\mu = 0.7$, where $|f_y| \leq \mu f_x$ and $f_x > 0$. The contact also has a restitution coefficient e , such that the pole-tip normal velocity relative to the wall before (v_N^-) and after (v_N^+) impact satisfies $v_N^+ = -ev_N^-$.

1) *Cost and Constraints in the Nominal Formulation:* Let $\mathbf{x} = [\mathbf{q}^\top, \dot{\mathbf{q}}^\top]^\top = [x, \theta, \dot{x}, \dot{\theta}]^\top$ denote the system state. The running cost is defined as

$$L_i = (\mathbf{x}_i - \mathbf{x}_{eq})^\top W_{\mathbf{x}} (\mathbf{x}_i - \mathbf{x}_{eq}) \Delta t_i + w_\tau \tau_i^2 \Delta t_i \quad (4)$$

where \mathbf{x}_{eq} denotes the equilibrium state, typically set to $\mathbf{x}_{eq} = [0, \pi, 0, 0]^\top$. The weighting matrices are chosen as $W_{\mathbf{x}} = \text{diag}(10, 10, 1, 1)$ and $w_\tau = 1$, representing the relative importance of state and control costs, respectively. No terminal cost is applied in this formulation. The initial and terminal boundary conditions are set as $\mathbf{x}_0 = \mathbf{x}_{\text{init}}$ and $\mathbf{x}_N = \mathbf{x}_{\text{end}}$.

During free-motion phases, i.e., before and after contact, the system dynamics must satisfy:

$$\forall i \in [0, c) \cup (c, N-1] :$$

$$M(\mathbf{q}_i) \ddot{\mathbf{q}}_i + H(\mathbf{q}_i, \dot{\mathbf{q}}_i) = [1, 0]^\top \tau_i, \quad (5a)$$

$$\mathbf{x}_{i+1} = \mathbf{x}_i + \begin{bmatrix} \dot{\mathbf{q}}_i \\ \ddot{\mathbf{q}}_i \end{bmatrix} \Delta t_i, \quad (5b)$$

$$g(\mathbf{x}_i) = x_i + l \sin \theta_i - x_{\text{wall}} > 0. \quad (5c)$$

At contact ($i = c$), the system satisfies the guard condition:

$$g(\mathbf{x}_i) = x_i + l \sin \theta_i - x_{\text{wall}} = 0 \quad (6)$$

which triggers the corresponding state transition, implicitly defined by the following constraints:

$$M(\mathbf{q}_i) \ddot{\mathbf{q}}_i + H(\mathbf{q}_i, \dot{\mathbf{q}}_i) = [1, 0]^\top \tau_i + J_c^\top \mathbf{F}, \quad (7a)$$

$$|f_y| \leq \mu f_x, \quad (7b)$$

$$\mathbf{x}_{i+1} = \mathbf{x}_i + \begin{bmatrix} \mathbf{0} \\ \ddot{\mathbf{q}}_i \end{bmatrix} \Delta t_{\text{impact}}, \quad (7c)$$

$$J_{c,0}(\dot{\mathbf{q}}_{i+1} + e\dot{\mathbf{q}}_i) = 0 \quad (7d)$$

Here, (7a) and (7b) define the contact dynamics, where $\mathbf{F} = [f_x, f_y]^\top$ denotes the impact force acting on the pole tip, and $\Delta t_{\text{impact}} = 0.001$ s is the assumed impact duration (meaning the continuous forces act during the impact process, [18]). The velocity transition is enforced through (7c) and (7d), while the position transition is also incorporated in (7c). Note that $J_{c,0}$ denotes the first row of the contact Jacobian. Here, we assume that the position remains unchanged during the near-instantaneous contact event. Additional constraints are imposed to ensure that the left edge of the cart does not collide with the wall:

$$\forall i \in [0, N] : x_i - \frac{1}{2} w_{\text{cart}} > x_{\text{wall}}, \quad (8)$$

where $w_{\text{cart}} = 0.08$ m denotes the cart width.

2) *Cost and Constraints in SURE*: In addition to the running cost on the common trajectory (4), the running cost for nodes on the rejoining branches is defined as

$$L_{i,j} = (\mathbf{x}_{i,j} - \mathbf{x}_{eq})^\top W_{\mathbf{x}} (\mathbf{x}_{i,j} - \mathbf{x}_{eq}) + w_{\tau} \tau_{i,j}^2 \quad (9)$$

where the same weighting factors are used as in the nominal case. The free-motion dynamics for all $i \in [0, \mathcal{K}_e) \cup (\mathcal{K}_e, N-1]$ follow (5a) and (5b). When the system enters the branching phase, it must satisfy the following guard constraints:

$$i = \mathcal{K}_0 : \quad g(\mathbf{x}_i) = x_i + l \sin \theta_i - x_{\text{wall}} = d, \quad (10a)$$

$$i = \mathcal{K}_e : \quad g(\mathbf{x}_i) = x_i + l \sin \theta_i - x_{\text{wall}} = -d \quad (10b)$$

At $i = \mathcal{K}_0$, the pole tip reaches the right bound of the uncertainty range, while at $i = \mathcal{K}_e$, it reaches the left bound. For each node within the branching phase $i \in \mathcal{K}$, the state \mathbf{x}_i is considered the pre-impact state, and a corresponding post-impact state $\mathbf{x}_{i,0}$ is defined implicitly by \mathbf{x}_{i+1} in (7). Each branch in the rejoining phase (i.e., $\forall i \in \mathcal{K}, j \in [0, N_r-1]$) then evolves according to the free-body dynamics defined in (5a) and (5b). Finally, all nodes beyond the branching and rejoining phases must remain outside the broadened guard region:

$$\forall i \notin \mathcal{K} : \quad g(\mathbf{x}_i) = x_i + l \sin \theta_i - x_{\text{wall}} > d. \quad (11)$$

3) *Experiments and Results*: The trajectories generated by both nominal and SURE approaches are used as references to control the system in simulation, and their performance is compared to evaluate robustness. As the simulation platform, we developed a custom environment to reproduce the physical behavior of the cart-pole system and its interaction with the wall. For tracking the reference trajectory, a proportional-derivative (PD) controller with feedforward compensation is employed:

$$\tau(t) = \mathbf{k}_p(\mathbf{q}_{des}(t) - \mathbf{q}(t)) + \mathbf{k}_d(\dot{\mathbf{q}}_{des}(t) - \dot{\mathbf{q}}(t)) + \tau_{des}(t), \quad (12)$$

where $\mathbf{k}_p \in \mathbb{R}^2$ and $\mathbf{k}_d \in \mathbb{R}^2$ are the proportional and derivative gain vectors of the PD controller, respectively. Their values are calculated using a Linear Quadratic Regulator (LQR) design. $\mathbf{q}_{des}(t)$, $\dot{\mathbf{q}}_{des}(t)$, and $\tau_{des}(t)$ denote the desired position, velocity, and control input obtained from the optimized trajectories. For experiments with identical initial conditions, the cart-pole system employs identical PD controller gains.

We evaluate whether stabilization can still be achieved under two sources of uncertainty: perception uncertainty in the wall position and modeling uncertainty in the restitution coefficient. In each trial, the wall position and restitution coefficient are randomly sampled and held fixed. The system is released from an (often aggressive) initial condition, and the controller attempts to track the reference trajectory while exploiting wall contact for stabilization. A trial is considered successful only if all of the following criteria are satisfied:

- (i) After 10 seconds, the system reaches the target state.
- (ii) The pole tip contacts the wall no more than once.
- (iii) The pole does not fall to the ground.

TABLE I
EXPERIMENTAL RESULTS IN SIMULATION FOR THE CART-POLE SYSTEM

Initial Condition	State				Success Rate		
	x [m]	\dot{x} [m/s]	θ [rad]	$\dot{\theta}$ [rad/s]	Nominal	Robust Nominal	Trajectory Scheduling
1	0	π	0	5.5	58.5%	60.0%	75.0%
2	0	π	0	6.5	37.0%	43.0%	48.0%
3	0	3.53	-1.0	3.5	37.0%	57.0%	70.0%
4	0	3.45	-0.5	4.5	46.5%	61.0%	72.5%
Total					44.8%	55.3%	66.4%

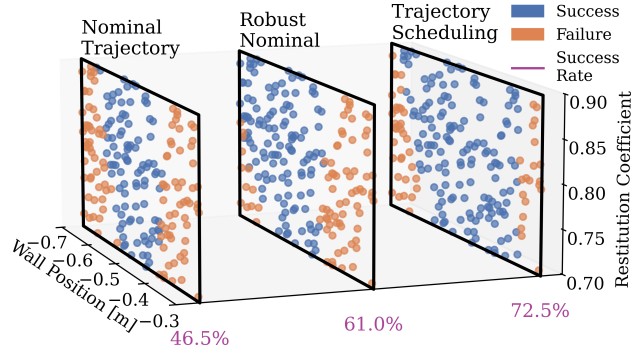


Fig. 5. Robustness comparison under Initial Condition 4 for three reference trajectories. The nominal wall position is $x_{\text{wall}} = -0.5$ m and the nominal restitution coefficient is 0.8. SURE trajectory optimization is performed using 5 branches, with the half-width of the uncertainty range fixed at $d = 0.05$ m. The wall position varies within $x_{\text{wall}} \in [-0.7$ m, -0.3 m], and the restitution coefficient ranges from 0.7 to 0.9. A total of 200 points are randomly sampled within this two-dimensional uncertainty space, and simulations are conducted for all three approaches to evaluate and compare their success rates.

(iv) The left edge of the cart does not penetrate the wall.

Four sets of initial conditions are evaluated. Each case starts from a different initial state but shares the same terminal state, $\mathbf{x}_{\text{end}} = [0, \pi, 0, 0]^\top$. For each case, we compare three reference trajectories: the nominal trajectory, the robust nominal trajectory (Section IV-C2), and the scheduled robust trajectories (Section IV-C1). The results are summarized in Table I, and representative successful and failed samples for Condition 4 are shown in Fig. 5.

First, we observe that the nominal trajectories already exhibit a certain degree of robustness to variations in wall position and restitution coefficient with a success rate of 44.8%, even though these uncertainties are not explicitly considered during optimization. In comparison, the SURE solution with trajectory scheduling demonstrates a substantially higher success rate of 66.4%—even when evaluated over a wider uncertainty range than that specified during optimization (the intended range being $e = 0.8$, $x_{\text{wall}} = -0.5 \pm 0.05$ m).

To further investigate whether the trajectory itself—*independent of the scheduler*—provides improved robustness, we compare the nominal trajectory with the robust nominal trajectory. In both cases, the controller is constrained to track a single deterministic reference. The results show that, even without a scheduler to accommodate different contact timings, the robust nominal trajectory exhibits an improvement in

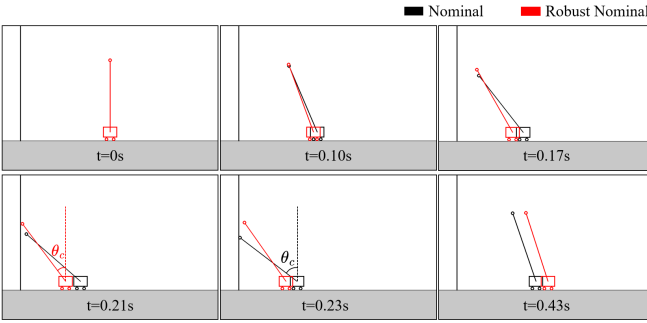


Fig. 6. Qualitative comparison between the nominal and robust nominal trajectories in simulation, with $\mathbf{x}_{\text{init}} = [0, \pi, 0, 5.5]^\top$ and $\mathbf{x}_{\text{end}} = [0, \pi, 0, 0]^\top$, assuming a nominal wall position of $x_{\text{wall}} = -0.5\text{m}$ and $d = 0.05\text{m}$. Here, θ_c denotes the pole angle at contact. Although both trajectories assume the same nominal wall position, they exhibit fundamentally different motion strategies when approaching the wall and when recovering balance. These differences directly affect the system's post-impact stability.

success rate (55.3%) compared to the nominal trajectory.

This suggests that the introduction of branching during trajectory optimization not only modifies the motion locally around the contact event but also reshapes the pre- and post-contact segments. As a result, the system adopts a more effective global motion strategy. This effect is illustrated in Fig. 6. In the nominal solution, the system knows the exact wall position; thus, the pole is allowed to swing freely as it approaches the wall. Around $t = 0.23\text{s}$, just before contact, the pole angle θ becomes excessively large, causing the pole to nearly collapse. The system then relies on a strong elastic rebound from the wall to recover its balance. In contrast, in the robust nominal solution, the cart begins moving leftward in coordination with the pole, preventing the pole angle from growing too large. At $t = 0.21\text{s}$, when contact occurs, the pole remains within a much smaller angular range, requiring only a mild impact to restore balance. Consequently, even if contact occurs slightly later than expected, the system can still maintain stability. After impact, the system shifts rightward to regain balance. Notably, the robust nominal solution exhibits a longer buffering distance, allowing additional room to compensate for discrepancies in contact timing or other uncertainties. These adjustments in the motion strategy explain the enhanced robustness of the robust nominal trajectory.

4) *Trade-off Between Optimality and Computing Time:* In addition to evaluating robustness, we also examine the computational cost of the proposed method. Figure 7 shows the computation time and resulting cost as functions of the number of nodes per branch (N_r), averaged over the four initial conditions in Table I.

Since not all configurations successfully converge to a solution, we first solve a simplified SURE trajectory optimization problem that is guaranteed to be feasible. The resulting solution is then used as an initial guess for solving the problem under the desired configuration. The reported computation time includes both the warm-start and solving phases. All analyses are conducted on a laptop running Ubuntu 24.04, equipped with an Intel Core Ultra 9 185H CPU and 32 GB of

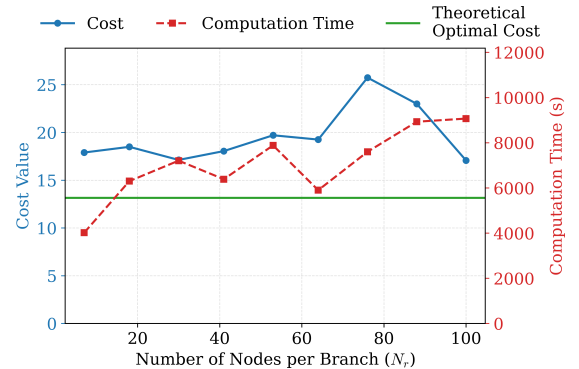


Fig. 7. Optimality-Computation Trade-off. For all configurations, the total number of nodes post-impact (i.e. the nodes on each branch plus the common final trajectory) is fixed at 100. The leftmost sample corresponds to the configuration adopted in this paper, which uses $N_r = 7$ nodes per branch and 93 nodes on the common final trajectory. The rightmost sample corresponds to the Tree OCP QP formulation introduced in Fig. 2c, in which the branches do not rejoin and each branch independently uses 100 nodes to propagate directly to the terminal state. The results show that increasing N_r does not lead to a significant reduction in cost, whereas the computation time increases rapidly.

RAM.

From the solution of the SURE trajectory optimization problem, we compute the actual wall position associated with each branch based on its pre-impact state. Using each inferred wall position as a deterministic wall location, we then solve a nominal trajectory optimization problem. This yields a nominal cost value for each branch; taking the average of these values gives an average cost, shown as the green line in Fig. 7. This represents the theoretical optimal cost for this problem with perfect knowledge.

Compared to Tree OCP QP(rightmost sample), forcing all branches to rejoin a common final trajectory introduces additional constraints, which leads to a higher cost. However, the results show that this loss in optimality is small, while the reduction in computation time is substantial – at $N_r = 7$ (leftmost sample), the cost increased by only 4.87% while the computation time decreased by 55.85%.

B. Case Study II: Ball Catching

As shown in Fig. 1, we consider a Unitree Z1 robotic manipulator with a lightweight container as its end effector. The manipulator dynamics are given by:

$$M(\mathbf{q})\ddot{\mathbf{q}} + H(\mathbf{q}, \dot{\mathbf{q}}) = \boldsymbol{\tau} \quad (13)$$

where $\mathbf{q} \in \mathbb{R}^6$ denotes the joint angles, $M(\mathbf{q}) \in \mathbb{R}^{6 \times 6}$ is the mass matrix, and $H(\mathbf{q}, \dot{\mathbf{q}}) \in \mathbb{R}^6$ collects the Coriolis, centrifugal, and gravitational terms. $\boldsymbol{\tau} \in \mathbb{R}^6$ is the vector of joint torques. A ball falls freely from an initial height h_0 with uncertainty $\pm d$ and no horizontal velocity. Given a prescribed release time, the manipulator aims to catch the ball while minimizing impact and move it to a final position.

1) *Cost and Constraints in the Nominal Formulation:* Assuming that the ball mass is small relative to the effective mass of the robot arm, minimizing the impact can be approximated

by minimizing the relative velocity between the ball and the end effector at contact. Additionally, we can assume that the impact does not significantly affect the robot trajectory. Let $\mathbf{x} = [\mathbf{q}^\top, \dot{\mathbf{q}}^\top]^\top$ denote the system state, the cost function of the nominal trajectory optimization problem comprises two terms:

$$\min_{\mathbf{x}, \dot{\mathbf{q}}, \tau, \Delta t} \|\mathbf{v}_{\text{ball},c} - \mathbf{v}_{\text{ee},c}\|^2 + w_a \sum_{i=0}^{N-1} \ddot{\mathbf{q}}_i^2 \Delta t_i \quad (14)$$

The first term penalizes the squared relative velocity between the ball and the end effector at the contact node c , where $\mathbf{v}_{\text{ball},c} \in \mathbb{R}^3$ and $\mathbf{v}_{\text{ee},c} \in \mathbb{R}^3$ denote their Cartesian velocities. The latter is given by $\mathbf{v}_{\text{ee},c} = J_t(\mathbf{q}_c) \dot{\mathbf{q}}_c$, where $J_t(\mathbf{q}_i) \in \mathbb{R}^{3 \times 6}$ denotes the translational Jacobian. The second term penalizes the accumulated joint accelerations to promote smooth motion, with w_a denoting the corresponding weight. For all nodes except the last, we require

$$\forall i \in [0, N-1] : \mathbf{M}(\mathbf{q}_i) \ddot{\mathbf{q}}_i + \mathbf{H}(\mathbf{q}_i, \dot{\mathbf{q}}_i) = \boldsymbol{\tau}_i, \quad (15a)$$

$$\mathbf{x}_{i+1} = \mathbf{x}_i + \begin{bmatrix} \dot{\mathbf{q}}_i \\ \ddot{\mathbf{q}}_i \end{bmatrix} \Delta t_i, \quad (15b)$$

$$1 - \mathbf{R}_{\text{ee},i} [0, 0, 1]^\top < \varepsilon, \quad (15c)$$

$$\|(\mathbf{p}_{\text{ee},i} - \mathbf{p}_{\text{ball},0})_{xy}\|^2 < \varepsilon. \quad (15d)$$

Here, (15a)–(15b) enforce the manipulator dynamics and a forward-Euler state update. To ensure reliable catching, (15c) enforces that the container bottom remains horizontal, and (15d) constrains the end-effector center to remain aligned with the ball's vertical trajectory. $\mathbf{p}_{\text{ball},0}$ denotes the ball's initial position, and $(\cdot)_{xy}$ denotes projection onto the x - y plane. $\mathbf{p}_{\text{ee},i}$ and $\mathbf{R}_{\text{ee},i}$ are the translational and rotational components of the end effector pose, respectively, computed via forward kinematics. Rather than enforcing (15c) and (15d) to be exactly zero, we impose inequality tolerances with $\varepsilon = 10^{-3}$, which improves numerical conditioning and accelerates convergence. The guard condition is defined as the vertical separation between the ball and the end-effector bottom. Prior to contact, the ball must remain above the end effector:

$$\forall i \in [0, c) : g(\mathbf{x}_i) = p_{\text{ball},i,z} - r_{\text{ball}} - p_{\text{ee},i,z} > 0, \quad (16)$$

where $p_{(\cdot),z}$ denotes the z -component of position and r_{ball} is the ball radius. At contact, the guard becomes zero and the contact event is triggered:

$$i = c : g(\mathbf{x}_i) = p_{\text{ball},i,z} - r_{\text{ball}} - p_{\text{ee},i,z} = 0. \quad (17)$$

The ball is assumed to remain attached to the end effector after contact. The pre-impact ball kinematics are given by

$$\mathbf{v}_{\text{ball},i} = \mathbf{v}_{\text{ball},0} + [0, 0, -g t_i]^\top, \quad (18a)$$

$$\mathbf{p}_{\text{ball},i} = \mathbf{p}_{\text{ball},0} + \mathbf{v}_{\text{ball},0} t_i + [0, 0, -\frac{1}{2} g t_i^2]^\top, \quad (18b)$$

where $\mathbf{v}_{\text{ball},0}$ is the initial ball velocity (typically zero) and t_i is the accumulated time at node i , $t_i = t_0 + \sum_{k=0}^{i-1} \Delta t_k$.

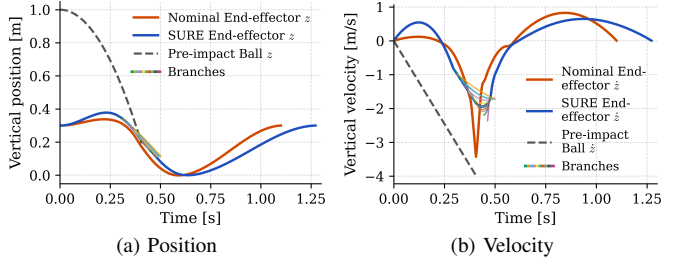


Fig. 8. Nominal trajectory: The end effector moves upward only slightly and then descends rapidly, anticipating contact at a deterministic time. SURE robust nominal trajectory: The end effector initially moves higher, enabling a longer co-travel distance with the egg. During descent, it follows a smoother, gradually accelerating motion, thereby accommodating the possibility of earlier or later contact.

2) *Cost and Constraints in SURE*: The free-motion dynamics for all $i \in [0, \mathcal{K}_e] \cup (\mathcal{K}_e, N-1]$ follow (15a) and (15b). Because the ball's initial height is uncertain, the formulation must account for a range of possible contact times. The earliest contact corresponds to the lowest initial height, whereas the latest contact corresponds to the highest initial height; all other feasible contact times lie between these two extremes. Over the branching phase, the following constraints are imposed:

$$i = \mathcal{K}_0 : g(\mathbf{x}_i) = p_{\text{ball},i,z} - r_{\text{ball}} - p_{\text{ee},i,z} = d, \quad (19a)$$

$$i = \mathcal{K}_e : g(\mathbf{x}_i) = p_{\text{ball},i,z} - r_{\text{ball}} - p_{\text{ee},i,z} = -d, \quad (19b)$$

$$\forall i \in \mathcal{K} : \|\mathbf{v}_{\text{ee},i} - \mathbf{v}_{\text{ball},i}\|^2 \leq v_{\text{lim}}^2, \quad (19c)$$

Here, (19a) and (19b) enforce the guard condition at the first and last nodes of the branching phase, respectively. At each branching node, (19c) bounds the relative velocity between the ball and the end effector, where $v_{\text{lim}} > 0$ denotes the upper bound on the allowable relative speed. The cost function in the robust optimization problem then minimizes this bound together with the accumulated joint accelerations:

$$\min_{\mathbf{x}, \dot{\mathbf{x}}, \Delta t, v_{\text{lim}}} v_{\text{lim}} + w_a \sum_{i=0}^{N-1} \ddot{\mathbf{q}}_i^2 \Delta t_i + w_a \sum_{i \in \mathcal{K}} \sum_{j=0}^{N_r-1} \ddot{\mathbf{q}}_{i,j}^2 \Delta t_{i,j} \quad (20)$$

For each branching node $i \in \mathcal{K}$, we assume state continuity at contact ($\mathbf{x}_{i,0} = \mathbf{x}_i$) and enforce that the corresponding branch rejoins the common final trajectory at its final node. Each branch evolves according to (15). Prior to the branching phase, we enforce that contact cannot occur prematurely, (16).

3) *Solution Results*: Figure 8 compares the solution trajectories obtained from the nominal and SURE optimization formulations, including the corresponding position and velocity profiles. The end effector starts from $\mathbf{p}_{\text{ee},0} = [0, 0, 0.3] \text{ m}$, catches the ball, and finally moves to $\mathbf{p}_{\text{ee},e} = [0, 0, 0.3] \text{ m}$. The ball is released from $\mathbf{p}_{\text{ball},0} = [0, 0, 1.0] \text{ m}$. In the SURE formulation, ten branches are generated and the half-width of the uncertainty in the initial height is set to $d = 0.20 \text{ m}$.

To further analyze impact robustness, we evaluate the relative velocity between the ball and the end effector at contact for different initial ball heights, as shown in Fig. 9. The results indicate that the robust nominal trajectory provides

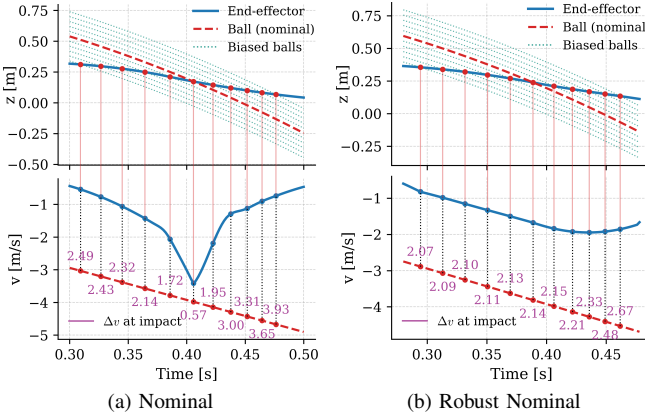


Fig. 9. Relative velocity between the ball and the end effector under varying initial ball heights. The ball is released from 11 uniformly spaced initial heights in the range $[p_{\text{ball},0,z} - 0.2 \text{ m}, p_{\text{ball},0,z} + 0.2 \text{ m}]$. The top row shows the vertical position profiles of the end effector and balls, while the bottom row shows the corresponding velocity profiles. Vertical dashed lines indicate the contact times for each trial, and the purple annotations report the relative velocity at impact. (a) Nominal trajectory, with a maximum impact relative velocity of 3.93m/s. (b) Robust nominal trajectory, with a reduced maximum impact relative velocity of 2.67m/s.

substantially improved robustness. The nominal trajectory performs well only when the ball is released from the nominal height; deviations in the initial height lead to higher relative velocities at contact for all but the nominal and two closest heights. In contrast, the robust nominal trajectory keeps the relative velocity v_{lim} bounded below 2.67 m/s across all tested initial heights, effectively limiting impact despite uncertainty in contact timing. Meanwhile, the nominal trajectory reaches a maximum relative velocity of 3.93 m/s (47% higher).

4) *Real-world Experiments*: We conduct physical experiments in which the robot attempts to catch an egg using either the nominal or the SURE robust nominal trajectory shown in Fig. 8, under identical initial conditions. The trajectory scheduling was not implemented as it requires accurate contact event sensing, which was not available at the time. As shown in Fig. 1, to perform controlled experiments, the egg is released by a second robot (a Franka Emika Panda) mounted on a higher table. The Unitree Z1 robot is mounted on a lower table opposite the Panda and performs the catching motion. At the start of each trial, the Z1 moves to an initial configuration in which the end effector is positioned directly beneath the egg. Both robots are connected to a laptop running Ubuntu 20.04 with a real-time kernel and remain idle until a trigger signal is issued. Upon receiving the signal, the Panda opens its gripper to release the egg, and the Z1 begins tracking the corresponding trajectory.

Opening the Panda gripper requires a non-negligible amount of time. Consequently, the Z1 must wait for a fixed delay $t_{\text{wait}} \approx 0.12\text{s}$ to achieve approximate synchronization. Ideally, this delay would align the start of the egg drop with the start of the catching motion. However, perfect synchronization is not achievable in practice due to multiple sources of timing uncertainty, including gripper actuation delay, communication

TABLE II
RESULT OF THE EGG DROP EXPERIMENT

t_{wait}	Trajectory	1	2	3	4	5	6	7	8	9	10	Success Rate
0.125s	nominal	✗	✓	✓	○	○	✗	○	✗	✗	✗	35%
	SURE	✓	✓	✓	✓	✓	✓	✓	○	✓	✓	95%
0.118s	nominal	✗	✗	✓	✓	✗	✓	✓	○	✓	✗	55%
	SURE	✓	○	○	✗	○	✓	✓	✓	✓	✓	75%
Total		nominal										45%
		SURE										85%

and processing latency, and controller timing discretization. We exploit this inherent uncertainty to evaluate the robustness of the proposed trajectories.

For each trajectory, we tune t_{wait} such that the average contact time is close to the nominal contact time. This is achieved by iteratively adjusting t_{wait} and performing ten drop-catch trials until the number of early contacts approximately equals the number of late contacts. After calibration, we obtain $t_{\text{wait}} = 0.118\text{s}$ for the nominal trajectory and $t_{\text{wait}} = 0.125\text{s}$ for the SURE trajectory. Using both of these delays, we conduct ten additional trials for each trajectory. We classify the outcomes of each trial into three categories:

- (i) successful catch without egg damage (score +1, denoted as ✓);
- (ii) egg contacts the end effector, bounces upward by more than 10 cm, then falls back into the end effector (by luck) without breaking (score +0.5, denoted as ○);
- (iii) egg breaks or falls to the ground (score 0, denoted as ✗).

The experimental results are summarized in Table II. The results show that, under both timing settings, the SURE trajectory consistently outperforms the nominal trajectory by achieving a higher success rate. Overall, SURE achieves an 85% success rate compared to 45% for the nominal approach, corresponding to a 40% improvement in egg-catching performance under timing uncertainty.

VI. CONCLUSION

In this paper, we proposed an efficient formulation for robust trajectory optimization that can handle uncertainties in contact timing. The main novelty of our formulation lies in branching possible solutions at different contact timings and rejoining all solutions at a common point outside the uncertain region. Through extensive simulation and experimental demonstrations, we showed that our framework adapts its strategy in the presence of uncertainty, resulting in more robust solutions than a nominal formulation at a lower computational cost than other robust approaches.

In future work, we plan to extend our formulation to account for imperfections in low-level control. Furthermore, we are interested to learn uncertainty-conditioned policies from our robust formulation under various uncertainty conditions. We are also interested in extending the framework to floating-base systems, with the goal of enabling robust loco-manipulation behaviors.

REFERENCES

[1] Bernardo Aceituno-Cabezas, Carlos Mastalli, Hongkai Dai, Michele Focchi, Andreea Radulescu, Darwin G Caldwell, José Cappelletto, Juan C Grieco, Gerardo Fernández-López, and Claudio Semini. Simultaneous contact, gait, and motion planning for robust multilegged locomotion via mixed-integer convex optimization. *IEEE Robotics and Automation Letters*, 3(3):2531–2538, 2017.

[2] Joel AE Andersson, Joris Gillis, Greg Horn, James B Rawlings, and Moritz Diehl. Casadi: a software framework for nonlinear optimization and optimal control. *Mathematical Programming Computation*, 11(1):1–36, 2019.

[3] Alp Aydinoglu, Adam Wei, Wei-Cheng Huang, and Michael Posa. Consensus complementarity control for multi-contact MPC. *IEEE Transactions on Robotics*, 2024.

[4] Miroslav Bogdanovic, Majid Khadiv, and Ludovic Righetti. Learning variable impedance control for contact sensitive tasks. *IEEE Robotics and Automation Letters*, 5(4):6129–6136, 2020.

[5] Miroslav Bogdanovic, Majid Khadiv, and Ludovic Righetti. Model-free reinforcement learning for robust locomotion using demonstrations from trajectory optimization. *Frontiers in Robotics and AI*, 9:854212, 2022.

[6] Julyan HE Cartwright and Oreste Piro. The dynamics of runge–kutta methods. *International Journal of Bifurcation and Chaos*, 2(03):427–449, 1992.

[7] Michal Ciebielski, Victor Dhédin, and Majid Khadiv. Task and motion planning for humanoid locomanipulation. In *IEEE-RAS International Conference on Humanoid Robots*, pages 1179–1186, 2025.

[8] Robin Deits and Russ Tedrake. Footstep planning on uneven terrain with mixed-integer convex optimization. In *IEEE-RAS International Conference on Humanoid Robots*, pages 279–286, 2014.

[9] Victor Dhédin, Haizhou Zhao, and Majid Khadiv. Simultaneous contact sequence and patch planning for dynamic locomotion. In *IEEE-RAS International Conference on Humanoid Robots*, pages 245–252, 2025.

[10] Luke Drnach and Ye Zhao. Robust trajectory optimization over uncertain terrain with stochastic complementarity. *IEEE Robotics and Automation Letters*, 6(2):1168–1175, 2021.

[11] Gianluca Frison and Moritz Diehl. HPIPM: a high-performance quadratic programming framework for model predictive control. *IFAC-PapersOnLine*, 53(2):6563–6569, 2020.

[12] Ahmad Gazar, Majid Khadiv, Sébastien Kleff, Andrea Del Prete, and Ludovic Righetti. Nonlinear stochastic trajectory optimization for centroidal momentum motion generation of legged robots. In *The International Symposium of Robotics Research*, pages 420–435. Springer, 2022.

[13] Ahmad Gazar, Majid Khadiv, Andrea Del Prete, and Ludovic Righetti. Multi-contact stochastic predictive control for legged robots with contact locations uncertainty. *arXiv preprint arXiv:2309.04469*, 2023.

[14] Ruben Grandia, Fabian Jenelten, Shaohui Yang, Farbod Farshidian, and Marco Hutter. Perceptive locomotion through nonlinear model-predictive control. *IEEE Transactions on Robotics*, 39(5):3402–3421, 2023.

[15] Kevin Green, Ross L Hatton, and Jonathan Hurst. Planning for the unexpected: Explicitly optimizing motions for ground uncertainty in running. In *IEEE International Conference on Robotics and Automation*, pages 1445–1451, 2020.

[16] Bilal Hammoud, Majid Khadiv, and Ludovic Righetti. Impedance optimization for uncertain contact interactions through risk sensitive optimal control. *IEEE Robotics and Automation Letters*, 6(3):4766–4773, 2021.

[17] Peter C Horak and Jeff C Trinkle. On the similarities and differences among contact models in robot simulation. *IEEE Robotics and Automation Letters*, 4(2):493–499, 2019.

[18] Aaron M Johnson, Samuel A Burden, and Daniel E Koditschek. A hybrid systems model for simple manipulation and self-manipulation systems. *The International Journal of Robotics Research*, 35(11):1354–1392, 2016.

[19] Aaron M Johnson, Jennifer E King, and Siddhartha Srinivasa. Convergent planning. *IEEE Robotics and Automation Letters*, 1(2):1044–1051, 2016.

[20] Gijeong Kim, Dongyun Kang, Joon-Ha Kim, Seungwoo Hong, and Hae-Won Park. Contact-implicit model predictive control: Controlling diverse quadruped motions without pre-planned contact modes or trajectories. *The International Journal of Robotics Research*, 44(3):486–510, 2025.

[21] Nathan J Kong, J Joe Payne, James Zhu, and Aaron M Johnson. Saltation matrices: The essential tool for linearizing hybrid dynamical systems. *Proceedings of the IEEE*, 2024.

[22] Quentin Le Lidec, Wilson Jallet, Louis Montaut, Ivan Laptev, Cordelia Schmid, and Justin Carpentier. Contact models in robotics: a comparative analysis. *IEEE Transactions on Robotics*, 2024.

[23] Joonho Lee, Jemin Hwangbo, Lorenz Wellhausen, Vladlen Koltun, and Marco Hutter. Learning quadrupedal locomotion over challenging terrain. *Science robotics*, 5(47):eabc5986, 2020.

[24] Jingru Luo and Kris Hauser. Robust trajectory optimization under frictional contact with iterative learning. *Autonomous Robots*, 41(6):1447–1461, 2017.

[25] Carlos Mastalli, Wolfgang Merkt, Guiyang Xin, Jaehyun Shim, Michael Mistry, Ioannis Havoutis, and Sethu Vijayakumar. Agile maneuvers in legged robots: a predictive control approach. *arXiv preprint arXiv:2203.07554*, 2022.

[26] Avadesh Meduri, Paarth Shah, Julian Viereck, Majid Khadiv, Ioannis Havoutis, and Ludovic Righetti. Bi-ConMP: A nonlinear model predictive control framework

for whole body motion planning. *IEEE Transactions on Robotics*, 39(2):905–922, 2023.

[27] David D Morrison, James D Riley, and John F Zanca naro. Multiple shooting method for two-point boundary value problems. *Communications of the ACM*, 5(12): 613–614, 1962.

[28] Amir Patel, Stacey Leigh Shield, Saif Kazi, Aaron M Johnson, and Lorenz T Biegler. Contact-implicit trajectory optimization using orthogonal collocation. *IEEE Robotics and Automation Letters*, 4(2):2242–2249, 2019.

[29] Brahayam Ponton, Majid Khadiv, Avadesh Meduri, and Ludovic Righetti. Efficient multicontact pattern generation with sequential convex approximations of the centroidal dynamics. *IEEE Transactions on Robotics*, 37(5):1661–1679, 2021.

[30] Holger Scheel and Stefan Scholtes. Mathematical programs with complementarity constraints: Stationarity, optimality, and sensitivity. *Mathematics of Operations Research*, 25(1):1–22, 2000.

[31] Yuki Shirai, Devesh K Jha, Arvind U Raghunathan, and Diego Romeres. Chance-constrained optimization for contact-rich systems using mixed integer programming. *Nonlinear Analysis: Hybrid Systems*, 52:101466, 2024.

[32] Marc Toussaint, Jason Harris, Jung-Su Ha, Danny Driess, and Wolfgang Hönig. Sequence-of-constraints MPC: Reactive timing-optimal control of sequential manipulation. In *IEEE/RSJ International Conference on Intelligent Robots and Systems*, pages 13753–13760, 2022.

[33] Marc A Toussaint, Kelsey Rebecca Allen, Kevin A Smith, and Joshua B Tenenbaum. Differentiable physics and stable modes for tool-use and manipulation planning. In *Robotics: Science and Systems*, 2018.

[34] Jari Van Steen, Gijs Van Den Brandt, Nathan van de Wouw, Jens Kober, and Alessandro Saccon. Quadratic programming-based reference spreading control for dual-arm robotic manipulation with planned simultaneous impacts. *IEEE Transactions on Robotics*, 40:3341–3355, 2024.

[35] Andreas Wächter and Lorenz T Biegler. On the implementation of an interior-point filter line-search algorithm for large-scale nonlinear programming. *Mathematical programming*, 106(1):25–57, 2006.

[36] Yuquan Wang, Niels Dehio, Arnaud Tanguy, and Abderrahmane Kheddar. Impact-aware task-space quadratic-programming control. *The International Journal of Robotics Research*, 42(14):1265–1282, 2023.

[37] Patrick M Wensing, Michael Posa, Yue Hu, Adrien Escande, Nicolas Mansard, and Andrea Del Prete. Optimization-based control for dynamic legged robots. *IEEE Transactions on Robotics*, 40:43–63, 2023.

[38] Lei Yan, Theodoros Stouraitis, Joao Moura, Wenfu Xu, Michael Gienger, and Sethu Vijayakumar. Impact-aware bimanual catching of large-momentum objects. *IEEE Transactions on Robotics*, 40:2543–2563, 2024.

[39] Haizhou Zhao and Majid Khadiv. Trajectory optimization under contact timing uncertainties. In *IEEE-RAS International Conference on Humanoid Robots*, pages 1064–1071, 2024.

[40] James Zhu, Nathan J Kong, George Council, and Aaron M Johnson. Hybrid event shaping to stabilize periodic hybrid orbits. In *IEEE International Conference on Robotics and Automation*, pages 01–07, 2022.

[41] James Zhu, J Joe Payne, and Aaron M Johnson. Convergent iLQR for safe trajectory planning and control of legged robots. In *IEEE International Conference on Robotics and Automation*, pages 8051–8057, 2024.

APPENDIX

A. Derivation of Dynamics Models of Cart Pole System

As illustrated in Figure 10, the pole is assumed to be massless, with its mass m_p concentrated at the tip and connected to the cart by a rigid, massless rod of length l . An external force $\mathbf{F} = [f_x, f_y]^\top$ acts on the pole tip.

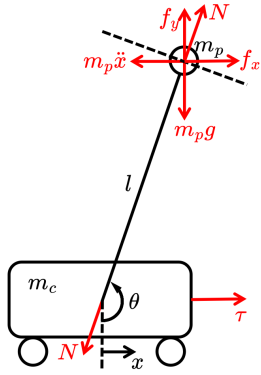


Fig. 10. Cart Pole System with External Force

According to the force equilibrium equation of the cart in the x -direction,

$$\sum F_x^{cart} = \tau - N \sin \theta = m_c \ddot{x} \quad (21)$$

From the moment equilibrium equation of the pole about the cart center,

$$\begin{aligned} & \sum M^{pole} \\ &= -m_p l \ddot{x} \cos \theta - m_p g l \sin \theta + f_x l \cos \theta + f_y l \sin \theta \quad (22) \\ &= m_p l^2 \ddot{\theta} \end{aligned}$$

From the force equilibrium in the centripetal direction,

$$\begin{aligned} & \sum F_{centripetal}^{pole} \\ &= -m_p g \cos \theta + m_p \ddot{x} \sin \theta - N - f_x \sin \theta + f_y \cos \theta \\ &= m_p l \dot{\theta}^2 \quad (23) \end{aligned}$$

From (23), the normal reaction N can be expressed as

$$N = -m_p g \cos \theta + m_p \ddot{x} \sin \theta - f_x \sin \theta + f_y \cos \theta - m_p l \dot{\theta}^2 \quad (24)$$

Substituting (24) into (21) yields

$$\begin{aligned} & \tau - m_p \ddot{x} \sin^2 \theta + m_p g \sin \theta \cos \theta \\ &+ f_x \sin^2 \theta - f_y \sin \theta \cos \theta + m_p l \dot{\theta}^2 \sin \theta \quad (25) \\ &= m_c \ddot{x} \end{aligned}$$

Applying algebraic manipulation, (25) becomes

$$\begin{aligned} & \tau - m_p \ddot{x} \sin^2 \theta - m_p \ddot{x} \cos^2 \theta + m_p \ddot{x} \cos^2 \theta \\ &+ m_p g \sin \theta \cos \theta + f_x \sin^2 \theta + f_x \cos^2 \theta - f_x \cos^2 \theta \\ &- f_y \sin \theta \cos \theta + m_p l \dot{\theta}^2 \sin \theta \\ &= m_c \ddot{x} \quad (26) \end{aligned}$$

Simplifying, we obtain

$$\begin{aligned} & \tau + m_p \ddot{x} \cos^2 \theta + m_p g \sin \theta \cos \theta \\ &+ f_x - f_x \cos^2 \theta - f_y \sin \theta \cos \theta \\ &+ m_p l \dot{\theta}^2 \sin \theta \\ &= (m_c + m_p) \ddot{x} \end{aligned} \quad (27)$$

This can be rewritten as

$$\begin{aligned} & \tau + f_x \\ &+ (m_p \ddot{x} \cos \theta + m_p g \sin \theta - f_x \cos \theta - f_y \sin \theta) \cos \theta \\ &+ m_p l \dot{\theta}^2 \sin \theta \\ &= (m_c + m_p) \ddot{x} \end{aligned} \quad (28)$$

From (22), we can derive

$$m_p \ddot{x} \cos \theta + m_p g \sin \theta - f_x \cos \theta - f_y \sin \theta = -m_p l \ddot{\theta} \quad (29)$$

Substituting (29) into (28) gives

$$(m_c + m_p) \ddot{x} + m_p l \ddot{\theta} \cos \theta - m_p l \dot{\theta}^2 \sin \theta = \tau + f_x \quad (30)$$

Additionally, (22) can be rewritten as

$$m_p l \ddot{x} \cos \theta + m_p l^2 \ddot{\theta} + m_p g l \sin \theta = f_x l \cos \theta + f_y l \sin \theta \quad (31)$$

By combining (30) and (31), the system dynamics can be expressed in matrix form as

$$\begin{bmatrix} m_c + m_p & m_p l \cos \theta \\ m_p l \cos \theta & m_p l^2 \end{bmatrix} \ddot{\mathbf{q}} + m_p l \sin \theta \begin{bmatrix} -\dot{\theta}^2 \\ g \end{bmatrix} = \begin{bmatrix} 1 \\ 0 \end{bmatrix} \tau + \begin{bmatrix} 1 & 0 \\ l \cos \theta & l \sin \theta \end{bmatrix} F \quad (32)$$

where $\mathbf{q} = [x, \theta]^\top$ and $\begin{bmatrix} 1 & 0 \\ l \cos \theta & l \sin \theta \end{bmatrix} = J_c^\top$ is the transpose of the contact Jacobian of the pole tip.

B. Implementation of the Cart-Pole with Wall Simulation

As the simulation environment, we develop a custom framework to reproduce the physical behavior of the cart-pole system and its interaction with the wall. When a collision between the pole tip and the wall is detected, the projected Gauss-Seidel (PGS) algorithm [17, 22] is employed to solve the nonlinear complementarity problem (NCP) at contact:

Algorithm 1: Projected Gauss-Seidel (PGS) Algorithm for NCP

Input: Delassus matrix: $G = J_c M(\mathbf{q})^{-1} J_c^\top$, pole tip velocity: $\mathbf{g} = J_c \dot{\mathbf{q}}$
Output: Contact force: \mathbf{F}
for $k = 1$ **to** n_{iter} **do**

$$\begin{cases} f_x \leftarrow f_x - \frac{1}{G_{xx}} (G\mathbf{F} + \mathbf{g} + e\mathbf{g})_x; \\ f_x \leftarrow \max(0, f_x); \\ f_y \leftarrow f_y - \frac{1}{G_{yy}} (G\mathbf{F} + \mathbf{g} + e\mathbf{g})_y; \\ f_T^{(i)} \leftarrow \text{proj}_{\mu f_x}(f_y); \end{cases}$$

end

Here, n_{iter} denotes the maximum number of iterations, set to 30 in this work. The term eg accounts for contact elasticity. The algorithm outputs the contact force \mathbf{F} , which is then used to update the system dynamics. The next-step state of the cart–pole system, during both free motion and contact, is computed using the Runge–Kutta integration method [6].

C. Design of the PD Controller for the Cart-Pole System

To compute the proportional and derivative gain vectors of the PD controller, $\mathbf{k}_p \in \mathbb{R}^2$ and $\mathbf{k}_d \in \mathbb{R}^2$, we employ a Linear Quadratic Regulator (LQR) design. The equations of motion of the open-loop system are first expressed in state-space form. Since the controller is only designed for trajectory tracking, the external force term \mathbf{F} in Equation 3 is neglected. The resulting nonlinear system can be written as

$$\begin{aligned} \dot{\mathbf{x}} &= \begin{bmatrix} x \\ \dot{x} \\ \theta \\ \dot{\theta} \end{bmatrix} = f(\mathbf{x}, u) \\ &= \begin{bmatrix} \dot{x} \\ \frac{m_p g \sin(\theta) \cos \theta + m_p l \sin \theta \cdot \dot{\theta}^2 + \tau}{m_c + m_p \sin^2 \theta} \\ \dot{\theta} \\ \frac{-(m_c + m_p)g \sin \theta - (m_p l \sin \theta \cdot \dot{\theta}^2 + \tau) \cos \theta}{(m_c + m_p \sin^2 \theta)l} \end{bmatrix} \end{aligned} \quad (33)$$

where $\mathbf{x} = [x, \dot{x}, \theta, \dot{\theta}]^\top$ is the system state vector and $u = \tau$ is the control input.

The system is linearized around the equilibrium point $\mathbf{x}_{eq} = [0, 0, \pi, 0]^\top$ and $u_{eq} = 0$, yielding the linearized dynamics

$$\dot{\mathbf{x}} = A\mathbf{x} + \mathbf{b}u \quad (34)$$

where the system matrices are defined as

$$A = \left. \frac{\partial f}{\partial \mathbf{x}} \right|_{\mathbf{x}_{eq}, u_{eq}}, \quad \mathbf{b} = \left. \frac{\partial f}{\partial u} \right|_{\mathbf{x}_{eq}, u_{eq}} \quad (35)$$

The state and control weighting matrices for the LQR design are chosen as

$$Q = \begin{bmatrix} 10 & 0 & 0 & 0 \\ 0 & 0 & 0 & 0 \\ 0 & 0 & 10 & 0 \\ 0 & 0 & 0 & 0 \end{bmatrix} \quad (36)$$

$$r = 0.1 \quad (37)$$

No cost is assigned to the velocity terms to prevent the controller from being overly aggressive in avoiding wall contact. Although this choice renders Q semi-positive-definite, it proves adequate for achieving stable and consistent performance during execution. The Riccati matrix P is then obtained by solving the continuous-time algebraic Riccati equation:

$$A^\top P + PA - P\mathbf{b}r^{-1}\mathbf{b}P + Q = 0 \quad (38)$$

Finally, the optimal state-feedback control law is expressed as

$$u = -K\mathbf{x}_{err} = -r^{-1}\mathbf{b}P\mathbf{x}_{err} \quad (39)$$

where \mathbf{x}_{err} is the state error. The proportional and derivative gains can then be extracted from the resulting feedback gain vector $K = [\mathbf{k}_p^\top, \mathbf{k}_d^\top]^\top \in \mathbb{R}^4$.